analytical chemistry

pubs.acs.org/ac Article

Etching Triangular Silver Nanoparticles by Self-generated Hydrogen Peroxide to Initiate the Response of an Electrochemiluminescence Sensing Platform

Jingwei Xue, Yue Jia, Lei Yang, Jinhui Feng, Dan Wu, Xiang Ren,* Yu Du,* Huangxian Ju, and Qin Wei

Cite This: https://dx.doi.org/10.1021/acs.analchem.0c03398 Read Online

ACCESS | Metrics & More | Article Recommendations | Supporting Information

ABSTRACT: This work outlines a versatile and high-performance electrochemiluminescence (ECL) platform that uses complex luminescent molecules [Ru(II) complex] formed by carbohydrazide (CON_4H_6) and tris(4,4′-dicarboxylicacid-2,2′-bipyridyl)ruthenium(II) dichloride [$Ru(dcbpy)_3^{2+}$] as emitters to facilitate the intramolecular ECL mechanism for reducing the response distance and interference, and they were kept immobilized on a porous bismuth vanadate nanoarray ($BiVO_4$ NA) to improve the orderliness of electron transfer. In addition, the detection was made depending on the etching of triangular silver nanoparticles (T-Ag NPs) by self-generated hydrogen peroxide (H_2O_2) to initiate the recovery response of the originally quenched ECL due to ECL-RET between the Ru(II) complex (donor) and T-Ag NPs (receptor). Because of the antibacterial application of dopamine, its own redox ability could produce more H_2O_2 for etching receptor T-Ag NPs under near-infrared (NIR) stimulation. Notably, in this system, the specific binding of antigens and antibodies with the autogenesis process of H_2O_2 and the ECL detection procedure are independent. Therefore, the proposed system can avert the impact of complex biological samples effectively, and the ECL efficiency of the Ru(II) complex can be readily utilized. On this basis, a biosensor is explored for the primary diagnosis of squamous cell carcinoma by detecting the biomarker named after cytokeratin fragment 19 (CYFRA21-1), from which an excellent linearity from 0.1 pg/mL to 50 ng/mL is achieved with a detection limit of 0.058 pg/mL. All of these results confirmed that this strategy can be a promising candidate for fabricating an ECL-based biosensor.

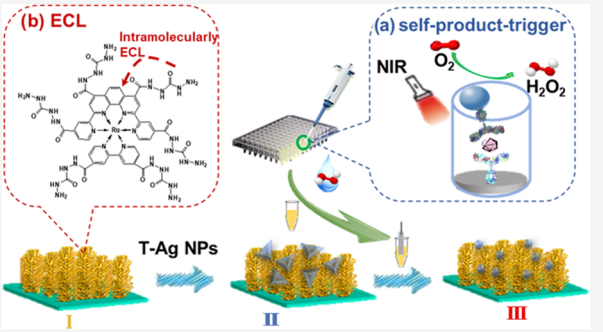

A biosensor, an instrument that is sensitive to biological substances and converts its concentration into electrical signals, is developed to play a vital role to detect trace levels of disease markers in early clinical diagnosis or prognosis.[1−5] Electrochemiluminescence (ECL) strategies have been extensively established for trace analysis considering the preponderances of high sensitivity, simple facility, wide dynamic range, and controllable switchers.[6−10] The sandwich design strategy is the most popular structure type of the ECL system. However, it often makes the process complex and thus difficult to commercialize, and the interference of accumulation by complex biotin on one detection electrode to the ECL emitter signal could not be negligible.[11,12] Therefore, to solve the defects caused by all the assembly processes on a single electrode,[13] the proposed novel technology, which includes a couple of autocephalous moieties of the ECL detection device and the specific binding of immune molecules with etching agent molecular release performed in 96 microporous plates, has been developed to avoid these shortcomings. This method, which greatly simplifies the ECL sensor interface, can serve as a significant, promising, and emerging analytical technique for current biomedical applications.

The etching susceptibility of triangular silver nanoparticles (T-Ag NPs) toward hydrogen peroxide (H_2O_2) leads us to think deeply.[14] T-Ag NPs, possessing strong ultraviolet light absorption ability, have been gaining attention due to their tremendous capacity for applications in sensing and diagnosis of diseases. Inspired by the potential of biomimetic redox-active antimicrobial coating in inhibiting bacterial contamination application, we are intrigued by the method of reducing nanomaterial accumulation and producing the target product in situ.[15] More interestingly, H_2O_2 generation depending on the redox state of PDA and further enhancement by its reduced state (PDA-red) and near-infrared irradiation (NIR) are reported as a product of enzyme catalysis.[16] From what has been discussed above, an efficient and novel strategy of ECL resonance energy transfer (ECL-RET) is proposed,[17] with

Received: August 11, 2020
Accepted: September 21, 2020
Published: September 21, 2020

Scheme 1. Synthesis Route of the Ru(II) Complex (A) and the Fabrication of the Self-produced Triggered System and the ECL Sensing Interface of this Biosensor (B)

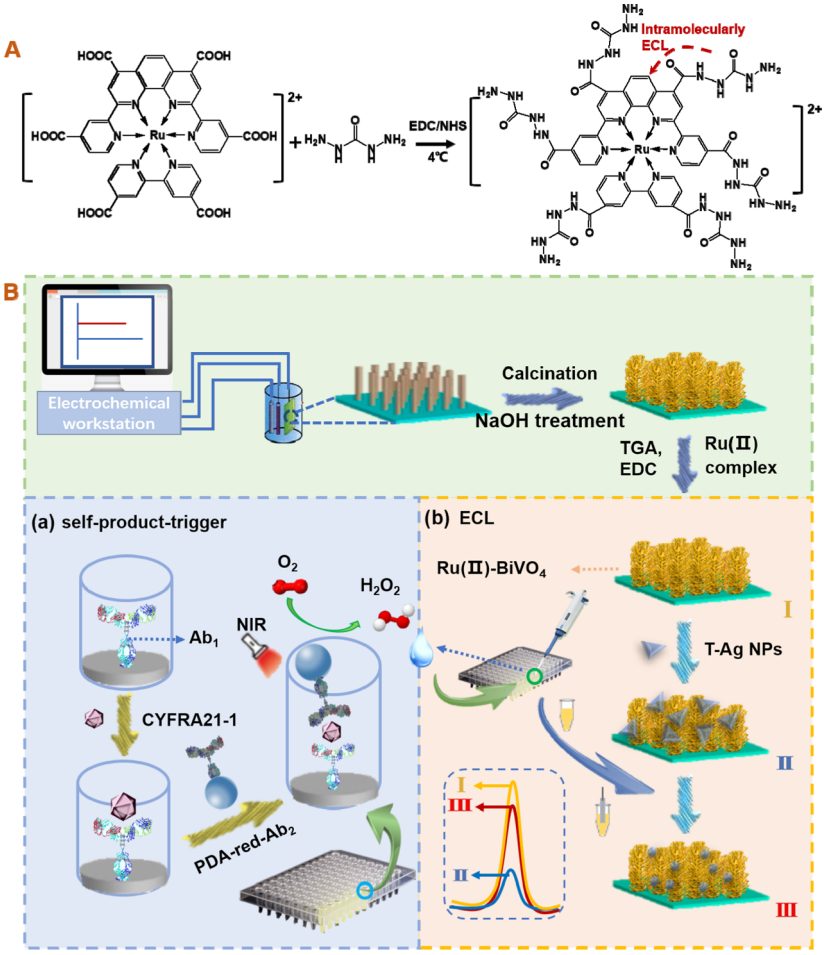

intramolecular ECL emission of the Ru(II) complex between carbohydrazide and tris(4,4′-dicarboxylicacid-2,2′-bipyridyl)-ruthenium(II) [$Ru(dcbpy)_3^{2+}$] as the ECL probe (donor) and T-Ag NPs as the ECL quencher (acceptor).[6] They are immobilized on a porous coral-like bismuth vanadate nanoarray ($BiVO_4$ NA), which could accelerate the reaction process between the signal label and the electrolyte due to the electron transfer along the ordered array structure.[18−20] Subsequently, on the basis of the self-produced triggered ECL turn-on strategy of the T-Ag/Ru(II)-$BiVO_4$ system, the ECL interface has been established successfully (Scheme 1).

There are several advantages presented by the proposed self-produced triggered ECL turn-on strategy. First, the architecture of the T-Ag/Ru(II)-$BiVO_4$ sensing interface is separated from the complex self-produced triggers; thus, the probe-modified interface can avoid the accompanying effect of spatial steric hindrance associated with the antibody labeled by the luminophore and the influence of complex biological samples to make ECL more efficient.

Furthermore, due to the synergistic amplification of signal by ECL technology, specific binding technique, and quenching recovery strategy, the high sensitivity detection can be realized better. Moreover, for the ECL part, intramolecular ECL emission of the Ru(II) complex not only reduces the uncertainty interference caused by the coreactant in solution but also shortens the response distance between the reaction agent and the emitter. Notably, the satisfying performance of this developed strategy is confirmed by employing cytokeratin fragment 19 (CYFRA21-1),19,20 a credible biomarker for the primary diagnosis of squamous cell carcinoma, as the real antigen analysis target, and the detection limit was obtained at 0.058 pg/mL. As expected, the multifunctional ECL interface detection system is sensitive, efficient, facile, convenient, and easily recyclable and can be applied in a straightforward manner direct detection of trace biomarkers in complex serum samples. As a consequence, this work not only broadens the role of a combination of diverse analytical methods to optimize the sensing interface but also supplies a universally promising self-produced triggered ECL detection model with high performance.

EXPERIMENTAL SECTION

Preparation of T-Ag NPs. In 96 mL of pure water, 200 μL of 50 mM $AgNO_3$ was added under magnetic agitation. Then, 2 mL of trisodium citrate (75 mM) and 100 μL of H_2O_2 (30%) were added. After that, rapid injection of 1 mL of $NaBH_4$ (100 mM) for the reduction was initiated in the solution, which immediately turned the solution to light yellow. When the solution color led to deep purple, it resulted in the formation of T-Ag NPs.[21]

Preparation of the ECL Sensing Interface. The prepared ITO/$BiVO_4$ NAs were immobilized according to our previous method.[22,23] Through the action of electrostatic adsorption and match between the bonds of Bi−S, in turn,

https://dx.doi.org/10.1021/acs.analchem.0c03398
Anal. Chem. XXXX, XXX, XXX−XXX

eligible concentrations of the Ru(II) complex and T-Ag were added to the electrode surface to combine with each other and set aside to form T-Ag/Ru(II)-$BiVO_4$/ITO.

Preparation of the Self-produced Triggered System. First, 1 mL of 50 ng/mL protein A solution was added to the above solution and oscillated for 1 h at 4 °C. Then, 100 μL of capture antibody (Ab_1, 1 μg/mL) was incubated in a 96-microwell plate overnight at 4 °C. After centrifugation at 12 000 rpm, the sediment was dispersed into 1 mL of PBS (pH 7.4). Then, 100 μL of 0.1% BSA solution was added to block the nonspecific active sites. After centrifugation and washing, 100 μL of different concentrations of CYFRA21-1 was added to the solution after washing. Then, 100 μL of PDA-red-Ab_2 was incubated at 37 °C for 1 h. Followed by centrifugation and washing again, the obtained bioconjugate was dissolved in 1 mL of ultrapure water. Afterward, it was treated with gentle shaking for 1 h and kept in the dark for 10 h (and NIR irradiation for 20 min).

Procedures for Detection of H_2O_2 Production. For the H_2O_2 assay, T-Ag/ITO was simply immersed in various incubation fluids in a 96-well microporous plate with different concentrations of self-produced H_2O_2 for 40 min. Afterward, the H_2O_2-disposed electrodes were fetched, washed, and dried under a N_2 atmosphere, and then the supernatant was taken to observe the changes by self-produced H_2O_2.

Procedures for Immunoassay. Referring to the self-produced triggered system, the resulting solution in each well of a 96 microporous plate was shifted to a tube for centrifugation, and the T-Ag/Ru(II)-$BiVO_4$/ITO electrodes were immersed for 20 min in every centrifuge tube. Afterward, the working electrodes were washed and dried under a N_2 atmosphere for ECL measurements, and its procedure is exhibited in the Supporting Information.

Analysis for the Real Sample. Ten microliters of the serum sample was diluted in 100 mL of PBS (0.1 M, pH 7.4) for the pretreatment process of the sample. The detection was done according to the procedure described above except that the position of CYFRA21-1 in the serum sample was replaced after treatment. For this system, several clinical serum samples were collected from the hospital.

RESULTS AND DISCUSSION

Material Characterization. First of all, the crystallization of $BiVO_4$ is characterized by X-ray diffraction (XRD) (Figure 1A). Diffraction peaks are observed at 2θ = 15.140, 28.947, 30.548, 34.494, 46.034, 47.305, 50.314, and 58.530°, which respectively correspond to the (020), (121), (040), (200), (042), (132), (202), and (321) planes of $BiVO_4$, respectively. Scanning electron microscopy (SEM) is used to characterize its morphology (Figure 1B). The results show that the arrays are arranged in an orderly manner, coral-like (see the inset of Figure 1B), with small holes on the surface, which also provide evidence for their more extensive binding sites. The macro picture of the array formed by electroplating is also shown in the illustration in the lower right corner of Figure 1B. X-ray photoelectron spectroscopy (XPS) further proves the existence and chemical state of components. The XPS pattern results of the overall survey (A) and of separate elements belonging to Bi (B), V (C), and O (D) are illustrated in Figure 2. In Bi 4f

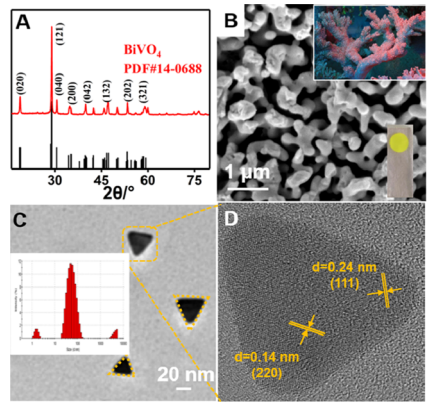

Figure 1. XRD pattern of $BiVO_4$ (A). SEM image of $BiVO_4$ (B). TEM (C), and HRTEM (D) images of T-Ag NPs.

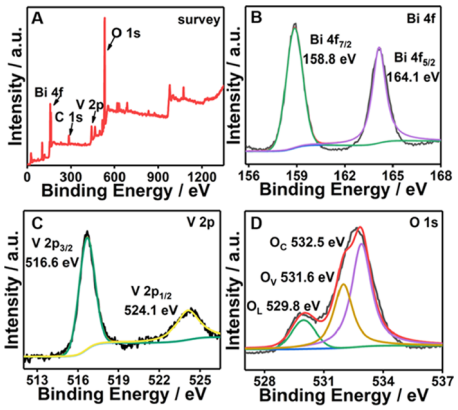

Figure 2. XPS pattern results of the overall survey (A) and of separate elements belonging to Bi (B), V (C), and O (D).

spectra, Bi $4f_{7/2}$ and Bi $4f_{5/2}$ pertain to the peaks of 158.8 and 164.1 eV, respectively.[24] The peaks of V 2p at 516.6 and 524.1 eV are allocated to the V $2p_{3/2}$ and V $2p_{1/2}$, respectively.[25] The peaks of O 1s, 529.8 eV, attributed to O_L, which is a lattice oxygen atom, 531.6 eV, subject to binding of the hydroxyl groups to metal cations in the oxygen-deficient region (O_V) and the dissociated oxygen species from H_2O (O_C) are attached to the peak of 532.5 eV.[26] SEM mapping (Figure S1D) reveals the existence and relatively uniform distribution of the three elements Bi (a), V (b), and O (c). All in all, the synthesis of the $BiVO_4$ nanoarray is successful. T-Ag NPs also applied the same characterization methods. As shown in Figure 1C, a transmission electron microscope (TEM) is used to observe the morphology. The form of the triangle is well displayed in the field of view. The particle size obtained by grain size analysis (inset) is approximately 43.3 nm, which is mutually confirmed with a high-resolution transmission electron microscope (HRTEM) (Figure 1D). After multiple magnification of this region, highly paralleled and ordered lattice fringes with a *d*-spacing of 0.24 and 0.14 nm are observed (Figure S1A) (Supporting Information), which is well in accordance with the (111) and (220) faces of Ag NP crystals. In addition, the SEM of polydopamine spheres (Figure S1B) obtained by dopamine self-polymerization is demonstrated in the Supporting Information.

Chemical Characterization of H_2O_2 Generation. According to the work of Liu's group,[15] depending on the redox state of PDA, H_2O_2 could be generated. Therefore, the formation of hydrogen peroxide was verified and monitored through the degradation of methylene blue by H_2O_2. The

https://dx.doi.org/10.1021/acs.analchem.0c03398
Anal. Chem. XXXX, XXX, XXX−XXX

specific detection status is shown in Figure 3A: the as-prepared PDA functional biocomplex is identified as PDA, the PDA

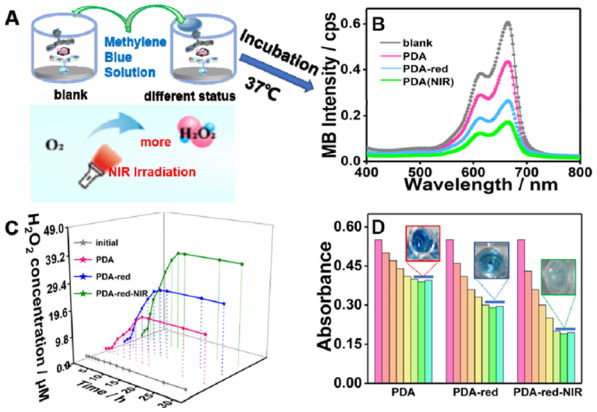

Figure 3. Diagram of methylene blue degradation (A), UV−vis spectrum of different samples (B), output of H_2O_2 production varies over time (C), and supported data by means of methylene blue degradation (D).

reduced with ascorbic acid is defined as PDA-red, the PDA reduced with NIR irradiation applied for 30 min is named as PDA-red-NIR, and one sample without PDA is compared as a blank sample (three groups were prepared). Then, the same concentration of methylene blue is added to these samples and kept standing for 12 h. After that, the supernatant is taken to observe the changes in the ultraviolet absorption (UV−vis) spectrum (Figure 3B). Three non-blank samples show a downward trend, that is, PDA can produce a certain amount of H_2O_2; PDA-red has a higher yield, and NIR irradiation can promote it. Besides, H_2O_2 production is tested over time with H_2O_2 kits (Figure 3C) and is supported by methylene blue degradation (Figure 3D), which has continuously increasing H_2O_2 levels during the 30 h incubation and shows a positive correlation, reaching the maximum value and tending to be stable after 10 h.

Possible Mechanisms of this ECL System. First of all, the ECL signals of electrodes to simple CON_4H_6 (a), simple $Ru(dcbpy)_3^{2+}$ (b), dispersion of CON_4H_6 into the electrolyte of $Ru(dcbpy)_3^{2+}$ (c), and the Ru(II) complex (d) are compared and explored (Figure 4A). The results clearly show that there is no signal of sample a, and the signals of simple b to d present a rising trend in turn. The comparison between sample c and sample d effectively indicates that carbohydrazide (CON_4H_6) can be used as a coreactant of $Ru(dcbpy)_3^{2+}$ to enhance the signals, and at the same time, the coreactant combined with $Ru(dcbpy)_3^{2+}$ can effectively improve the ECL signals, possibly because the distance between the emitter and the coreactant is shortened, energy consumption is reduced, and efficiency is improved. Therefore, this system is inferred from the general ammonia oxidation mechanism in the past;[27−29] the analysis equation is shown below

$$CON_4H_6 - Ru(II) - 2e^- \rightarrow CON_4H_6^{\cdot+} - Ru(III)$$

$$CON_4H_6^{\cdot+} - Ru(III) \rightarrow CON_4H_6^{\cdot} - Ru(III) + H^+$$

$$CON_4H_6^{\cdot} - Ru(III) \rightarrow CON_4H_6 - Ru(II)^*$$

$$CON_4H_6 - Ru(II)^* \rightarrow CON_4H_6 - Ru(II) + h\nu$$

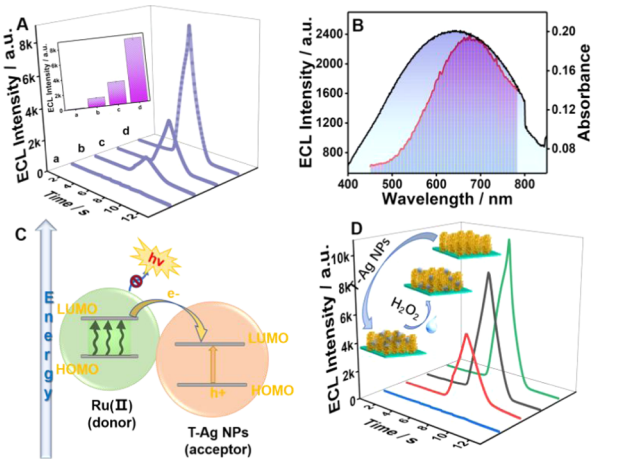

Figure 4. ECL signals of electrodes to simples (A), ECL intensity of the Ru(II) complex and the UV−vis spectrum of T-Ag NPs (B), ECL-RET mechanism process (C), and ECL signal recovery mechanism (D).

Then, for the quenching part, several probable mechanisms were speculated: (1) T-Ag NPs, owing to the expansive absorption spectrum, absorbed the ECL intensity of the Ru(II) complex and (2) the occurrence of RET was caused by appropriate energy level matching between T-Ag NPs and the Ru(II) complex. To thoroughly investigate and verify the specific ECL quenching mechanism responsible for the T-Ag NPs-mediated Ru(II) complex strategy, the following experiments were put into effect. First of all, the ECL emission range of the Ru(II) complex was observed at 500−800 nm with the maximum value of ∼675 nm and the UV−visible absorption of T-Ag NPs ranging from 400 to 900 nm with a peak of ∼655 nm. The relationship between these two cannot be neglected and has a tremendous influence on the ECL quenching process by Förster resonance energy transfer (Figure 4B). Afterward, the lowest unoccupied molecular orbital (LUMO) and the highest occupied molecular orbital (HOMO) energy levels of T-Ag NPs ($E1_{HOMO}$, $E1_{LUMO}$) and the Ru(II) complex ($E2_{HOMO}$, $E2_{LUMO}$) were also investigated by CV to explore the distribution of RET between T-Ag NPs and the Ru(II) complex. These values were, respectively, calculated to be −5.65 and −3.42 eV for the Ru(II) complex and −6.10 and −3.49 eV for T-Ag NPs, and the detailed process of calculation has been reflected in the Supporting Information (Figure S2). Because the $E2_{LUMO}$ of the Ru(II) complex was higher than the $E1_{LUMO}$ of T-Ag NPs, this opened up the possibility of electron transfer from the Ru(II) complex to T-Ag NPs, indicating that the ECL-RET process could not be ignored simultaneously in the proposed quenching system (Figure 4C). On the basis of all of the above, the satisfactory quenching effect should depend on the synergy of spectral overlap and energy level matching. This system uses ECL-RET between the Ru(II) complex and T-Ag NPs to generate quenching signals and adopts a signal recovery strategy to measure etching by self-produced H_2O_2. The state of the electrode surface and the ECL signals are disclosed in Figure 4D. Furthermore, in this way, the error is reduced and the sensitivity of the sensor is improved.

Increased Electroactive Surface Area of the $BiVO_4$ Nanoarray. To further prove that the $BiVO_4$ nanoarray has a large specific surface area, the electroactive area is measured by

https://dx.doi.org/10.1021/acs.analchem.0c03398
Anal. Chem. XXXX, XXX, XXX−XXX

cyclic voltammetry. The whole analysis depends on the Randles−Sevcik equation[30]

$$i_{ps} = 2.69 \times 10^5 n^{3/2} D^{1/2} v^{1/2} AC \quad (1)$$

$$A = \frac{k}{2.69 \times 10^5 n^{3/2} D_0^{1/2} C_0} \quad (2)$$

where i_{ps} is the peak reduction current of $K_3Fe(CN)_6$, n is the number of transferred electrons (n = 1), A is the electrochemical active area (cm^2) of the electrode, D refers to the diffusion coefficient of $K_3Fe(CN)_6$ (D_0 = 6.70 ± 0.02 ×10^{-6} cm^2/s), C refers to the concentration of $K_3Fe(CN)_6$ (C_0 = 2.5×10^{-3} mol/L), and v represents the scanning speed. Accordingly, the calculated electroactive area is 30.9 mm^2, which is effectively verified when compared with the precursor BIOI (A = 18.2 mm^2); it is found that $BiVO_4$ has a larger electroactive area, indicating stronger penetration and more reaction sites to promote the reaction rate and efficiency (Figure 5A).

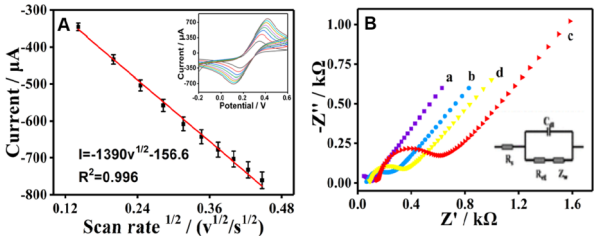

Figure 5. CV curve to detect the electroactive surface area and its linear relation (A) and EIS testing of the proposed sensing platform (B). Error bars = standard deviation (SD), (n = 3).

Electrochemical Impedance Spectroscopy (EIS) Characterization. For the assembly of the sensor interface, electrochemical impedance spectroscopy (EIS) is applied in electrochemical analysis.[31] The curves in Figure 5B represent bare ITO (a), Ru(II)-$BiVO_4$/ITO (b), T-Ag/Ru(II)-$BiVO_4$/ITO (c), and T-Ag/Ru(II)-$BiVO_4$/ITO after etching by the self-produced H_2O_2 solution (d), respectively. It can be observed that the impedance value obtained by sensing interface layer modification is much smaller than that in our previous work,[31] which further highlights the advantage of the low impedance of this immunoassay strategy. The etching process is further confirmed successfully by the comparison of T-Ag NPs before and after etching. The simulation parameters of the equivalent circuit components are shown in Table S1 (Supporting Information).

Performance Evaluation of the Proposed Biosensor. Compared with traditional biosensors directly modifying the immune molecules to be tested on the surface of the electrode, the proposed method of separating the specific recognition process from the detection process is more advantageous.[32] To evaluate one proposed sensing strategy, methods such as linear dependence, specificity, and stability toward the sensing platform, real sample analysis, and the like were always put forward.[33] This biosensor has a satisfactory linear correlation with the analyte to reflect its feasibility well (Figure 6A): ΔI_{ECL} = 2343.04 × log c + 8432.43 (correlation coefficient = 0.995) and a low detection limit at 0.058 pg/mL (S/N = 3), which is lower than some of the existing testing methods (Table S2). Based on this, substances common in serum as interferents are mixed with 0.1 ng/mL CRYRA21-1, and these mixtures are

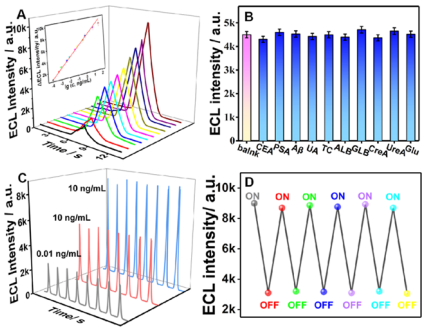

Figure 6. Original detection data of the signal and the standard curve with the changed values of the signals of this sensing interface (A), specificity tests of biosensors for 0.1 ng/mL CRYRA21-1 with interferents (B), stability tests in eight cycles (C), and recyclability of the ECL sensing platform (D). Error bars = SD, (n = 3).

made as targets. With the high consistency of the ECL intensity, all substances are produced without significant detection interference (Figure 6B). For the stability test of this sensor, the ECL−time curves are plotted in eight cycles for cyclic excitation of CRYRA21-1 with 0.01, 0.5, and 10 ng/mL (Figure 6C). In this case, the obtained signals have no obvious floating, so it can be concluded that the stability test results are satisfactory. More interestingly, the recyclability of this ECL sensing platform is found to be remarkable even after 10 rounds of soaking T-Ag/Ru(II)-$BiVO_4$/ITO in the self-produced solution containing H_2O_2 (Figure 6D), indicating its fast refreshing property.

Real Sample Analysis. To evaluate the practicality of the constructed ECL biosensor in the real samples, the standard addition method was applied here for the analysis of CYFRA21-1. The samples of normal human serum spiked with concentrations of 0.1, 2, 10, and 30 ng/mL were detected by the biosensor we developed. As shown in Table 1, the

Table 1. Recovery Results of CYFRA21-1 with Serum Samples

sample	addition content (ng/mL)	amount found (ng/mL)	recovery (%)
1	0.1	0.105	105
2	3	3.12	104
3	10	9.87	98.7
4	30	28.9	96.3

recovery data of the above were found from 93.2 to 103.5%. Therefore, the favorable accuracy and practicality of the proposed ECL biosensor were successfully proved. F-test and t-test results are shown in the Supporting Information.

CONCLUSIONS

Herein, a high-performance self-produced triggered ECL turn-on interface has been fabricated by coalescing the technology superiorities of the high-quantum yield Ru(II) complex, by taking advantage of the synergistic effect between the spectral overlap of the absorption−emission pairs and ECL-RET from the Ru(II) complex and T-Ag NPs. Moreover, relying on the etching of H_2O_2 produced by the PDA-red-based immune reaction on T-Ag NPs, the ECL biosensor interface with high sensitivity has been further improved. In addition, the proposed platform adopts a simply operated strategy of making immune steps and detection steps independent,

https://dx.doi.org/10.1021/acs.analchem.0c03398
Anal. Chem. XXXX, XXX, XXX−XXX

which effectively eliminates the influence of complex biological samples modified on the electrode surfaces and makes the ECL probe easy to be recycled. Based on these preponderances, the presented versatile platform is reputably facile and efficient with a wider dynamic range and lower detection limit and can be applied successfully for analyzing trace biomarkers in real serum samples. In general, this interface can hold extensive feasibility, which can help to broaden innovative designs to build sensing interfaces and bring new opportunities with reference values for biological analysis and clinical diagnosis.

■ ASSOCIATED CONTENT

Supporting Information

The Supporting Information is available free of charge at https://pubs.acs.org/doi/10.1021/acs.analchem.0c03398.

Materials and reagents; apparatus; synthesis of porous $BiVO_4$; synthesis of the Ru(II) complex; preparation of PDA and PDA-red-Ab_2; ECL measurement procedure; FTIR of the Ru(II) complex; calculation of the detection limit; *F*-test and *t*-test; XRD of T-Ag NPs; SEM of PDA; SEM of BiOI; and SEM mapping of $BiVO_4$ (PDF)

■ AUTHOR INFORMATION

Corresponding Authors

Xiang Ren − *Collaborative Innovation Center for Green Chemical Manufacturing and Accurate Detection, University of Jinan, Jinan 250022, P. R. China;* orcid.org/0000-0002-4321-4282; Email: chem_renx@163.com

Yu Du − *Collaborative Innovation Center for Green Chemical Manufacturing and Accurate Detection, University of Jinan, Jinan 250022, P. R. China*; Email: duyu_ujn@163.com

Authors

Jingwei Xue − *Collaborative Innovation Center for Green Chemical Manufacturing and Accurate Detection, University of Jinan, Jinan 250022, P. R. China*

Yue Jia − *Collaborative Innovation Center for Green Chemical Manufacturing and Accurate Detection, University of Jinan, Jinan 250022, P. R. China*

Lei Yang − *Collaborative Innovation Center for Green Chemical Manufacturing and Accurate Detection, University of Jinan, Jinan 250022, P. R. China*

Jinhui Feng − *Collaborative Innovation Center for Green Chemical Manufacturing and Accurate Detection, University of Jinan, Jinan 250022, P. R. China*

Dan Wu − *Collaborative Innovation Center for Green Chemical Manufacturing and Accurate Detection, University of Jinan, Jinan 250022, P. R. China;* orcid.org/0000-0002-8732-5988

Huangxian Ju − *Collaborative Innovation Center for Green Chemical Manufacturing and Accurate Detection, University of Jinan, Jinan 250022, P. R. China; State Key Laboratory of Analytical Chemistry for Life Science, Department of Chemistry, Nanjing University, Nanjing 210023, P. R. China;* orcid.org/0000-0002-6741-5302

Qin Wei − *Collaborative Innovation Center for Green Chemical Manufacturing and Accurate Detection, University of Jinan, Jinan 250022, P. R. China;* orcid.org/0000-0002-3034-8046

Complete contact information is available at: https://pubs.acs.org/10.1021/acs.analchem.0c03398

Notes

The authors declare no competing financial interest.

■ ACKNOWLEDGMENTS

This work was supported by the National Key Scientific Instrument and Equipment Development Project of China (No. 21627809); the National Natural Science Foundation of China (No. 21777056), the Jinan Scientific Research Leader Workshop Project (2018GXRC024), and the Special Foundation for Taishan Scholar Professorship of Shandong Province (No. ts201712052).

■ REFERENCES

(1) Luo, J.-H.; Cheng, D.; Li, P. X.; Yao, Y.; Chen, S. H.; Yuan, R.; Xu, W. J. *Chem. Commun.* **2018**, *54*, 2777−2780.
(2) Yang, L.; Fan, D.; Zhang, Y.; Ding, C.; Wu, D.; Wei, Q.; Ju, H. *Anal. Chem.* **2019**, *91*, 7145−7152.
(3) Yang, X.; Yu, Y. Q.; Peng, L. Z.; Lei, Y. M.; Chai, Y. Q.; Yuan, R.; Zhuo, Y. *Anal. Chem.* **2018**, *90*, 3995−4002.
(4) Zhou, Y.; Chen, S.; Luo, X.; Chai, Y.; Yuan, R. *Anal. Chem.* **2018**, *90*, 10024−10030.
(5) Sun, J.; Zhou, F.; Hu, H.; Li, N.; Xia, M.; Wang, L.; Wang, X.; Wang, G. *Anal. Chem.* **2020**, *92*, 6136−6143.
(6) Fu, L.; Zhang, B.; Fu, K.; Gao, X.; Zou, G. *Anal. Chem.* **2020**, *92*, 6144−6149.
(7) Jia, Y.; Yang, L.; Xue, J.; Zhang, N.; Fan, D.; Ma, H.; Ren, X.; Hu, L.; Wei, Q. *ACS Sens.* **2019**, *4*, 1909−1916.
(8) Wang, Y.-Z.; Ji, S. Y.; Xu, H. Y.; Zhao, W.; Chen, H. Y.; et al. *Anal. Chem.* **2018**, *90*, 3570−3575.
(9) Xue, J.; Yang, L.; Jia, Y.; Zhang, Y.; Wu, D.; Ma, H.; Hu, L.; Wei, Q.; Ju, H. *Biosens. Bioelectron.* **2019**, *142*, No. 111524.
(10) Anderson, T. J.; Defnet, P. A.; Zhang, B. *Anal. Chem.* **2020**, *92*, 6748−6755.
(11) Xue, J.; Yang, L.; Wang, H.; Yan, T.; Fan, D.; Feng, R.; Du, B.; Wei, Q.; Ju, H. *Biosens. Bioelectron.* **2019**, *133*, 192−198.
(12) Xue, J.; Yang, L.; Jia, Y.; Wang, H.; Zhang, N.; Ren, X.; Ma, H.; Wei, Q.; Ju, H. *ACS Sens.* **2019**, *4*, 2825−2831.
(13) Peng, H.; Huang, Z.; Wu, W.; Liu, M.; Huang, K.; Yang, Y.; Deng, H.; Xia, X.; Chen, W. *ACS Appl. Mater. Interfaces* **2019**, *11*, 24812−24819.
(14) Huang, L.; Yuan, C.; Chen, W.; Zeng, F.; Xu, H.; Zhang, Y.; Jiang, T. *ACS Nano* **2018**, *13*, No. 1850022.
(15) Liu, H.; Qu, X.; Tan, H.; Song, J.; Lei, M.; Kim, E.; Payne, G. F.; Liu, C. *Acta Biomater.* **2019**, *88*, 181−196.
(16) Song, J.; Liu, H.; Lei, M.; Tan, H.; Chen, Z.; Antoshin, A.; Payne, G. F.; Qu, X.; Liu, C. *ACS Appl. Mater. Interfaces* **2020**, *12*, 8915−8928.
(17) Wu, M. S.; Shi, H. W.; He, L. J.; Xu, J. J.; Chen, H. Y. *Anal. Chem.* **2012**, *84*, 4207−4213.
(18) Feng, J.; Li, F.; Liu, L.; Liu, X.; Wei, Q.; et al. *Sens. Actuators, B* **2020**, *308*, 127685−127692.
(19) Kammer, M. N.; Kussrow, A. K.; Webster, R. L.; Chen, H.; Hoeksema, M. D.; Christenson, R. H.; Massion, P. P.; Bornhop, D. J. *ACS Comb. Sci.* **2019**, *21*, 465−472.
(20) Li, Y.; Xuan, J.; Song, Y.; Qi, W.; He, B.; Wang, P.; Qin, L. *ACS Nano* **2016**, *10*, 1640−1647.
(21) Yang, X.; Yu, Y.; Gao, Z. *ACS Nano* **2014**, *8*, 4902−4907.
(22) Feng, J.; Li, F.; Qian, Y.; Sun, X.; Fan, D.; Wang, H.; Ma, H.; Wei, Q. *Sens. Actuators, B* **2020**, *305*, No. 127443.
(23) Yang, L.; Xue, J.; Jia, Y.; Zhang, Y.; Wu, D.; Ma, H.; Wei, Q.; Ju, H. *Biosens. Bioelectron.* **2019**, *142*, No. 111562.
(24) Xia, L.; Li, J.; Bai, J.; Li, L.; Zeng, Q.; Zhou, B.; et al. *Nanoscale* **2017**, *10*, 2848−2855.
(25) Dubal, D. P.; Kolleboyina, J.; Zboril, R.; Fischer, R. A.; Gomez-Romero, P. *J. Mater. Chem. A* **2018**, *6*, 6096−6106.
(26) Xu, R.; Lu, P.; Wu, B.; Wang, X.; Pang, X.; Du, B.; Fan, D.; Wei, Q. *Sens. Actuators, B* **2018**, *274*, 349−355.

https://dx.doi.org/10.1021/acs.analchem.0c03398
Anal. Chem. XXXX, XXX, XXX−XXX

(27) Witt, M. D.; Roughton, S.; Isakson, T. J.; Richter, M. M. *J. Lumin.* **2016**, *171*, 118−123.
(28) Zhou, Y.; Zhuo, Y.; Liao, N.; Chai, Y.; Yuan, R. *Talanta* **2014**, *129*, 219−226.
(29) Ji, J.; He, L.; Shen, Y.; Hu, P.; Li, X.; Jiang, L. P.; Zhang, J. R.; Li, L.; Zhu, J. J. *Anal. Chem.* **2014**, *86*, 3284−3290.
(30) Yang, L.; Jia, Y.; Wu, D.; Zhang, Y.; Ju, H.; Du, Y.; Ma, H.; Wei, Q. *Anal. Chem.* **2019**, *91*, 14066−14073.
(31) Xue, J.; Yang, L.; Du, Y.; Ren, Y.; Ren, X.; Ma, H.; Wu, D.; Ju, H.; Li, Y.; Wei, Q. *Sens. Actuators, B* **2020**, *321*, No. 128454.
(32) Gao, H.; Zhang, J.; Liu, Y.; Tu, W.; Dai, Z.; et al. *Anal. Chem.* **2019**, *91*, 12038−12045.
(33) Wu, F.-F.; Zhou, Y.; Zhang, H.; Yuan, R.; Chai, Y.-Q. *Anal. Chem.* **2018**, *90*, 2263−2270.

https://dx.doi.org/10.1021/acs.analchem.0c03398
Anal. Chem. XXXX, XXX, XXX−XXX